Antarctic Subglacial Trace Metal Mobility Linked to Climate Change Across Termination III

Gavin Piccione[1], Terrence Blackburn[2], Paul Northrup[3], Slawek Tulaczyk[2], Troy Rasbury[3]

[1]Department of Earth, Environmental, and Planetary Science, Brown University, Providence, 02912, USA
[2]Earth and Planetary Sciences, University of California Santa Cruz, Santa Cruz, 95064, USA
[3]Department of Geosciences, Stony Brook University, Stony Brook, 11794, USA

Correspondence to: Gavin Piccione (gavin_piccione@brown.edu)

Abstract. Antarctic meltwater is a significant source of iron that fertilizes present-day Southern Ocean ecosystems and may enhance marine carbon burial on geologic timescales. However, it remains uncertain how this nutrient flux changes through time, particularly in response to climate, due to an absence of geologic records detailing trace metal mobilization beneath ice sheets. In this study, we present a 25 kyr record of aqueous trace metal cycling beneath the East Antarctic Ice Sheet measured in a subglacial chemical precipitate that formed across glacial termination III (TIII). The deposition rate and texture of this sample describe a shift in basal meltwater flow following the termination. Alternating layers of opal and calcite deposited in the 10kyr prior to TIII record centennial-scale subglacial flushing events, whereas reduced basal flushing resulted in slower deposition of a trace metal-rich (Fe, Mn, Mo, Cu) calcite in the 15 kyr after TIII. This sharp increase in calcite metal concentrations following TIII indicates that diminished subglacial meltwater flow restricted the influx of oxygen from basal ice melt to precipitate-forming waters, causing dissolution of redox-sensitive trace metals from the bedrock substrate. These results are consistent with a possible feedback between orbital climate cycles and Antarctic subglacial iron discharge to the Southern Ocean, whereby heightened basal meltwater flow during terminations supplies oxygen to subglacial waters along the ice sheet periphery, which reduces the solubility of redox sensitive elements. As the climate cools, thinner ice and slower ice flow reduce basal meltwater production rates, limiting oxygen delivery and promoting more efficient mobilization of subglacial trace metals. Using a simple model to calculate the concentration of Fe in Antarctic basal water through time, we show that the rate of Antarctic iron discharge to the Southern Ocean is highly sensitive to this heightened mobility, and may therefore, increase significantly during cold climate periods.

1 Introduction

Southern Ocean (SO) biological productivity exerts a central influence on the concentration of CO_2 in the atmosphere by regulating the efficiency of the ocean biological pump (Sigman et al., 2010). Despite the SO comprising the largest sink of anthropogenic CO_2 (Sabine et al., 2004; Landschützer et al., 2015), modern primary productivity in this region is limited by the availability of iron (Fe) (Martin, 1990) and manganese (Mn) (Balaguer et al., 2022; Browning et al., 2021). During glacial periods in the past, increased Fe fertilization of SO phytoplankton supported elevated marine carbon burial and resulting

atmospheric CO_2 drawdown (Martínez-García et al., 2014; Jaccard et al., 2016; Martínez-Garcia et al., 2011). Glaciogenic aeolian dust is considered the primary source of the amplified Fe flux during cold climates (Martínez-Garcia et al., 2011; Shoenfelt et al., 2018); however, recent studies show that Antarctic meltwater (Herraiz-Borreguero et al., 2016; Gerringa et

35   al., 2012; Alderkamp et al., 2012; Annett et al., 2015a; Monien et al., 2017; Forsch et al., 2021; Dold et al., 2013; Hodson et al., 2017) and iceberg rafted detritus (Raiswell et al., 2008, 2016) contribute an equal or greater magnitude of bioavailable Fe to the modern ocean relative to aeolian dust (Hawkings et al., 2014, 2020). This suggests that discharge of trace metal-rich meltwater can significantly enhance SO primary productivity (Death et al., 2014) on geologic timescales.

Antarctic basal waters accumulate trace metals through abiotic water-rock interaction (Webster, 1994), biogeochemical

40   weathering of bedrock (Mikucki et al., 2009), and dissolution of ancient marine salt deposits (Lyons et al., 2019). Some combination of these processes produces high metal concentrations in perennially ice-covered lakes and subglacial aqueous environments in the McMurdo Dry Valleys (MDV), most notably in an 18 km long groundwater system beneath Taylor Valley that discharges at Blood Falls (Mikucki et al., 2015). It is unclear whether subglacial waters become enriched in trace metals elsewhere throughout Antarctica. In the absence of available data describing trace metal cycling beneath the broader ice sheet,

45   it is difficult to evaluate the total Antarctic flux of limiting nutrients like iron and manganese.

Throughout the continent-wide hydrologic system beneath the Antarctic ice sheet, melting of fresh basal ice is the lone source of oxygen to the ice-bed interface. Accordingly, areas with high basal melting and hydrological flushing rates will receive oxidized waters, while microbial utilization of oxygen in less hydrologically active regions can drive waters towards anoxia (Wadham et al., 2019; Livingstone et al., 2022). A simulation of modern subglacial melting shows that meltwater

50   production occurs primarily beneath the interior regions of the ice sheet and fast flowing ice streams, while thinner ice along Antarctic ice sheet edges prevents basal melting and drives cold-based conditions (Pattyn, 2010). Therefore, oxygen concentration in subglacial waters along the ice sheet periphery are likely controlled by the delivery of fresh melt from more interior regions, as is inferred for Subglacial Lake Whillans based on in situ measurements (Vick-Majors et al., 2016). Emerging evidence has described greater hydrologic flow from beneath the ice sheet interior to the margins during millennial-

55   scale warm periods (Piccione et al., 2022). This link between Southern Hemisphere climate and basal meltwater flow rates could influence the magnitude of trace metals released from the Antarctic subglacial environment across glacial-interglacial cycles by changing the redox conditions of marginal basal water.

Geochemical properties of Antarctic subglacial meltwater have been measured in Subglacial Lakes Whillans (Tulaczyk et al., 2014) and Mercer (Priscu et al., 2021), beneath two Antarctic ice streams (Skidmore et al., 2010), and at two basal

60   meltwater discharge sites (Goodwin, 1988; Lyons et al., 2019). Researchers speculate that chemical reactions governing trace element mobility in these contemporary waters may vary in response to ice dynamic changes, particularly as a consequence of future climate warming (Hawkings et al., 2020). Here, we present a 25 kyr record of hydrological and chemical conditions beneath the EAIS measured in a subglacial chemical precipitate that formed across glacial termination III (TIII): the rapid transition from glacial to interglacial climate conditions at the Marine Isotope Stage (MIS) 8-7 boundary between 251ka and

65   243ka. This sample provides a unique opportunity to examine the processes that govern Antarctic trace element mobility, and

to examine how climate change influences Antarctic basal meltwater supply and trace metal export. Using ^{234}U-^{230}Th carbonate dates to construct a depositional age model, we find that a prominent change in precipitate texture occurs across TIII. Variations in isotopic compositions (Sr, U, C, and O) and deposition rate across this boundary indicate a shift in the subglacial hydrologic system, where heightened meltwater flushing rates during TIII give way to less frequent flushing and greater isolation of

70   peripheral waters after the termination. Because of prolonged isolation following the glacial termination, precipitate parent waters exhibit a dramatic increase in trace metal concentrations. These data suggest that iron-rich subglacial waters, like those of Blood Falls (Lyons et al., 2019), can form as a natural consequence of ice thinning and deceleration during climate cooling events following terminations. Within this framework we outline potential feedback between climate cycles and subglacial trace element mobility, where reduced hydrologic activity following terminations cause subglacial waters to become suboxic

75   and triggers dissolution of redox sensitive elements from the underlying bedrock.

2 Methods

We report geochronological and geochemical data from sample PRR50504: a chemical precipitate that formed in water at the base of the Antarctic Ice Sheet. This sample was found at the ice surface at Elephant Moraine: a supraglacial moraine in a blue ice region on the East Antarctic side of the Transantarctic Mountains along the Ross Embayment. To get to the surface, it was

80   eroded from the ice-bed interface and entrained in basal ice, which exhumed in the blue ice area experiencing prolong sublimation (Kassab et al., 2019). This precipitate – a ~2 cm accumulation of opal and carbonate – consists of two distinct textures: the bottom 1.6cm of the sample is made up of ~200μm, alternating layers of white opal and tan carbonate, and the top 0.4 cm consists of brown carbonate with two black colored opal layers (Fig. 1a).

2.1 U-Series Geochronology

85   U-series ^{234}U-^{230}Th dates were produced for eight carbonate layers in sample PRR50504 at the University of California Santa Cruz (UCSC) Keck Isotope Laboratory following methods described in Blackburn et al., 2020 (Blackburn et al., 2020). Samples were separated into ~2mm slabs and carbonate was digested in 3mL 7N HNO$_3$, which dissolves carbonate but not opal layers. The solution was separated from undigested opal, and a mixed ^{229}Th-^{236}U tracer was added for isotope dilution analysis. U and Th separates were purified using ion chromatography with 1mL columns of 200-400 mesh, AG1-X8 anion

90   resin. Column wash acid was collected for later Sr measurements. Total procedural blanks were <10pg for U and <25pg for Th.

Uranium and thorium isotope measurements were conducted using the IsotopX X62 Thermal Ionization Mass Spectrometer (TIMS) housed at UCSC. Purified U and Th are loaded onto 99.99% purity Re ribbon, in silica gel and graphite emitters respectively. Uranium measurements were performed as a two sequence "Fara-Daly" routine: in the first sequence,

95   ^{234}U (mass 266) is collected on the Daly, while ^{235}U (mass 267) and ^{238}U (mass 270) is collected on the high Faraday cups equipped with 1e^{12} Ω resistors. The second sequence placed ^{235}U (mass 267) on the Daly and ^{236}U (mass 268) and ^{238}U (mass

270) on the high Faraday cups. The 266(Daly)/270(Faraday) composition was corrected using the Fara-Daly gain: (267Faraday/270Faraday) / (267Daly/270Faraday). Thorium was run as a metal and was measured using a peak hopping routine on the Daly. Thorium fractionation and deadtime were estimated by running NBS U-500 as a metal. Accuracy of ^{234}U-^{230}Th dates were tested using MIS 5e coral and compared to dates from (Hamelin et al., 1991), as well as a previously dated carbonate precipitate (Frisia et al., 2017). U-Th ages were calculated using codes designed at UCSC. All ages were corrected for initial $[^{230}$Th/ ^{232}Th] assuming a composition of 0.82 ± 0.4. Since the exact $[^{230}$Th/ ^{232}Th]$_i$ of our sample is unknown, we assume this ratio from the expected composition of the silicate upper crust in secular equilibrium, allowing for a departure from this composition of 50%, and propagating this uncertainty through to the final age. Decay constants for all data and models were from (Cheng et al., 2000). All uncertainties are reported at 2σ, unless otherwise specified.

We constructed an age model describing age versus sample depth using Chron.jl (Keller, 2018). There we input sample height and ^{234}U-^{230}Th dating dates into a Bayesian Markov chain Monte Carlo model that considers the age of each layer and its stratigraphic position within the sample to refine the uncertainty of each date using a prior distribution based on the principal of superposition (Fig. S1).

2.2 Isotope Analyses

2.2.1 Carbon and Oxygen Isotopes

Carbon and oxygen isotope ratios were measured by UCSC Stable Isotope Laboratory using a Thermo Scientific Kiel IV carbonate device and MAT 253 isotope ratio mass spectrometer. Referencing $\delta^{13}C_{CO3}$ and $\delta^{18}O_{CO3}$ to Vienna PeeDee Belemnite (VPDB) is calculated by two-point correction to externally calibrated Carrara Marble 'CM12' and carbonatite NBS-18 (Coplen et al., 2006). Externally calibrated coral 'Atlantis II' (Ostermann and Curry, 2000) was measured for independent quality control. Typical reproducibility of replicates was significantly better than 0.05 ‰ for $\delta^{13}C_{CO3}$ and 0.1 ‰ for $\delta^{18}O_{CO3}$.

2.2.2 Strontium Isotopes

Sr isotopic measurements were made on the TIMS at the UCSC Keck Isotope Laboratory using a one sequence, static measurement: ^{88}Sr was measured on the Axial Faraday Cup, while ^{87}Sr, ^{86}Sr, ^{85}Rb, and ^{84}Sr were measured on the low cups. Accuracy of the ^{87}Sr/^{86}Sr was evaluated using standard SRM987 compared to a long-term laboratory average value of 0.71024. with a typical reproducibility of ±0.00004‰. The absolute standard error for the precipitate Sr isotope measurements reported here are between 2.8e-5 and 4.8e-6.

2.3 Laser Ablation (LA ICP-MS) Elemental Analyses

Laser ablation inductively coupled plasma–mass spectrometry (LA ICP-MS) analyses were conducted at the Facility for Isotope Research and Student Training (FIRST) at Stony Brook University following protocols outlined in (Piccione et al., 2022). Analyses were made using a 213 UV New Wave laser system coupled to an Agilent 7500cx quadrupole ICP-MS. The

National Institute of Standards and Technology (NIST) 612 standard was used for approximate element concentrations using signal intensity ratios. Laser data were reduced in Iolite software (Paton et al., 2011); element concentrations were processed with the trace-element data reduction scheme in semiquantitative mode, which subtracts baselines and corrects for drift in
130 signal. Following acquisition, laser data representing calcite were isolated from those representing opal and detritus by subtracting points with Si concentration > 100,000ppm and with Al concentration > 400 ppm.

2.4 Synchrotron X-Ray Fluorescence (XRF) and X-Ray Absorption Near Edge Structure (XANES)

X-Ray Florescence (XRF) maps and X-ray absorption near-edge structure (XANES) analyses were made at the Tender Energy
135 X-ray Spectroscopy (TES) Beamline 8-BM (Northrup, 2019), and at the X-ray Fluorescence Microprobe (XFM) Beamline 4-BM at the National Synchrotron Light Source (NSLS-II) at Brookhaven National Laboratory. At TES, incident beam energy was set to 2700 eV with Si (111) monochromator crystals and focused to a 5×10 μm spot size for large elemental maps and for microbeam X-ray absorption spectroscopy and was reduced to 2×3 μm for fine mapping. Samples were oriented at 45° to beam, and fluorescence was measured using a Canberra ultra-low–energy Ge detector. The 2700 eV beam stimulates
140 fluorescence from elements Mg through S but is below the Ca K-edge to avoid interference. Sulfur K-edge XANES were collected over an energy of 2440-2550 eV, which stimulate fluorescence above the S K-edge but is below Ca K-edge to avoid interference. Energy scanning was conducted in quick on-the-fly mode, 10–30 seconds per scan with multiple scans at selected pixels of the elemental maps. At XFM, XRF maps were collected with the sample mounted at 45° relative to the micro-focused incident beam with a spot size of 5×8 μm. Data were collected using on-the-fly scanning with a 125 ms dwell time using a
145 four-element Vortex-ME4 silicon-drift-diode detector with incident energy tuned to 17.3 keV to stimulate fluorescence from elements Ca and heavier. XANES of Fe and Mn were measured by step-scanning energy across those elements' respective K absorption edges at 7.1 and 6.4 keV. Normalization and analysis of XANES spectra used the Athena software (Ravel and Newville, 2005).

2.5 Opal-Calcite Timeseries Analysis

150 We investigated the depositional timing of finely laminated opal-calcite layers in the bottom 1.6 cm of PRR50504 through spectral analyses of timeseries data that describe these mineralogic transitions. Starting with the XRF-element map of calcium (Fig. 2b), we measured a line scan of signal intensity across the precipitate layers to derive a spectrum representing mineralogy (i.e. high Ca layers represent calcite, low Ca layers represent opal; Fig. 2c). This spectrum was then plotted versus our age-depth model to produce a timeseries. To analyse the frequency of opal-calcite transitions in this timeseries, we used the
155 MATLAB signal multiresolution analyser app to generate decomposed frequency signals from the timeseries spectrum. The best match for the original spectra was produced with deconstructed signals with periods between 150 and 650 (Fig. 2b, c), indicating that opal-calcite layers were deposited with a centennial-scale frequency.

2.6 Model of Subglacial Meltwater Production and Relative Iron Discharge

To illustrate how Antarctic basal water melting and flux rates may have varied with climate and ice sheet fluctuations, we
160   use a simplified model of thermal energy balance beneath the Antarctic ice sheet (see Supplemental Materials section 1) (Fig. 1f). There are too many uncertainties, including the uncertainty in sample formation location, for us to make a meaningful attempt at simulating the specific variations that our precipitate sample has experienced. To appreciate the challenge with detailed modelling of past basal melting rates in Antarctica, one can examine the tremendous effort that it took Llubes et al. (2006) or Pattyn (2010) to derive estimates (with significant uncertainties) of melt rates beneath the modern, relatively well
165   constrained, configuration of the Antarctic ice sheet (Llubes et al., 2006; Pattyn, 2010). Hence, we opt for a simplified model that captures the salient aspects of climate-driven variations in subglacial melting rates (Supplementary Text). The implicit assumption in our approach is that the hydrological variations our sample experienced during its formation reflected the general subglacial hydrological conditions beneath the ice sheet.

We combine modelled subglacial meltwater production (Fig. 1f), with precipitate derived estimates of iron mobilization
170   to explore the change in Antarctic Fe flux to the Southern Ocean across TIII. First, we assume that the modelled rate of meltwater production in the subglacial environment is a reasonable estimate of discharge rate, given that the size of the hydrologic reservoir beneath the Antarctic ice sheet does not change considerably on a yearly basis, and thus the amount of water input to the system must be balanced by water export. We then calculate Fe discharge rate by setting the Fe concentration of these Antarctic basal waters. Based on our precipitate Fe concentrations, parent waters had minimal Fe prior to the
175   termination. Therefore, we set the concentrations of these waters equal to those of modern Subglacial Lake Whillans (2504nM), which contains dissolved oxygen and low concentrations of redox sensitive elements (Vick-Majors et al., 2020). As discussed below, post-TIII precipitate parent waters bear geochemical similarities to the contemporary Blood Falls brine, indicating that these metal-rich waters may form in the aftermath of glacial terminations and can affect Antarctic meltwater Fe flux. We simulate this additional Fe discharge by setting post-TIII subglacial water Fe concentration equal to Subglacial Lake Whillans
180   values, plus a range between 1 and 5% Fe equal to the concentration in the Blood Falls brine (4×10^6 nM).

3 Results and Discussion

3.1 Decreased Basal Meltwater Flushing Following Glacial Termination III

Using ^{234}U-^{230}Th carbonate dates along a transect from the top to the bottom of the sample, we constructed a model describing age versus sample height that constrains the depositional age of PRR50504 to a 25 kyr period between 259.2±2.15 ka and
185   224.8±1.51 ka (Fig. 1; Fig. S1). The carbonate and opal layers in the bottom section were deposited from 259.2±2.15 ka to 247±3.2 ka during the end of MIS 8. Following a depositional hiatus, the top carbonate formed from 239.7±2.55 ka to 224.8±1.51 ka during MIS 7 (Fig. 1b). Based on this age model, the boundary between the top and bottom sections of the sample represents an unconformity that occurred from 247±3.2 ka to 239.7±2.55 ka, coinciding with TIII (Fig. 1). The

190 interruption of precipitation could result from increased subglacial water flow during the termination, which would dilute subglacial waters with fresh meltwater and drive the parent solution below calcite saturation (Piccione et al., 2022) or from erosion of calcite during times of high meltwater flow (Wróblewski et al., 2017). In either case, the ~7.3 kyr between TIII and the resumption of carbonate precipitation represents the period over which parent waters became concentrated enough to reach carbonate saturation again.
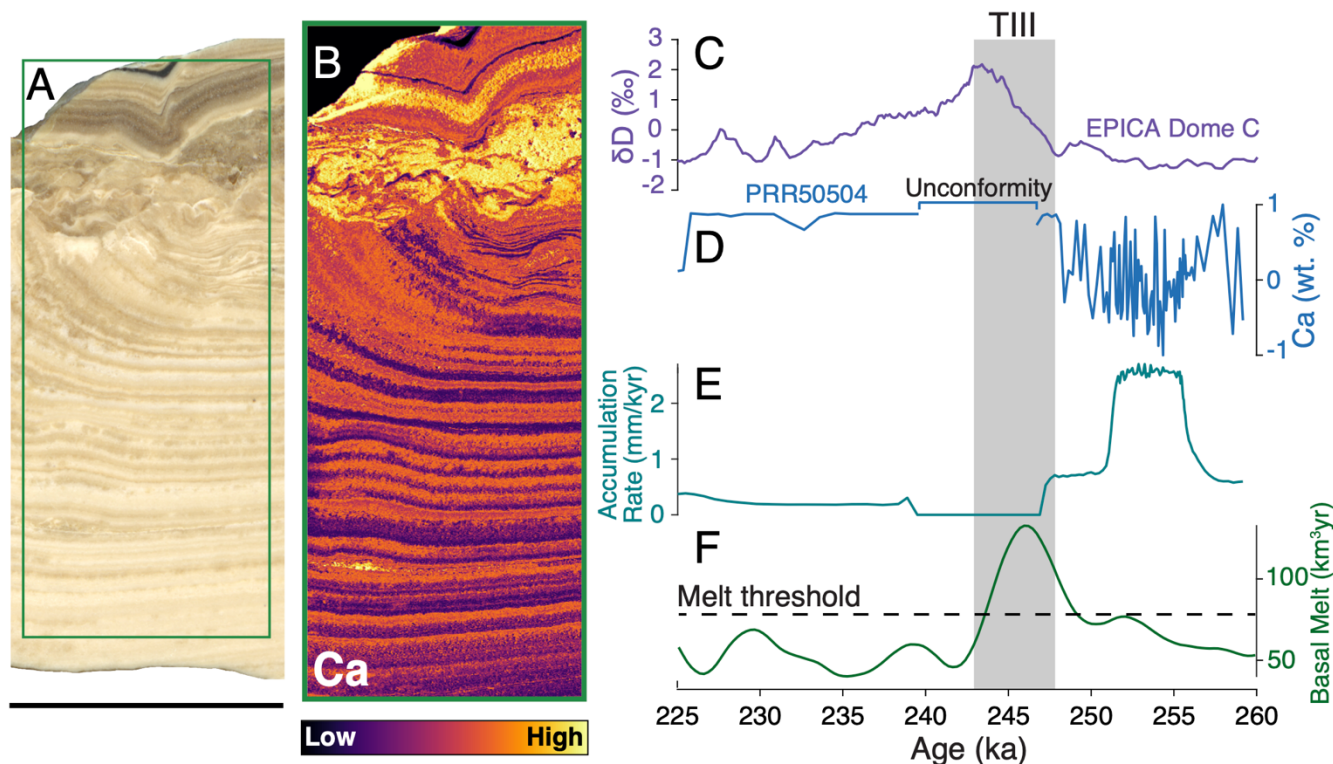
Figure 1 (below): Sample PRR50504 formation timeseries versus EPICA Dome C Ice Core Record. (A) Plain light image of sample
195 PRR50504. Green box delineates location of the elemental map shown in panel B**. (B)** µ-XRF map of Ca in PRR50504. **(C)** δD measured in the EPICA Dome C Ice Core **(Jouzel et al., 2007; Veres et al., 2013)**. (D) Timeseries of normalized Ca concentration in PRR50504. High Ca values represent carbonate layers; low Ca values represent opal layers. (E) Calculated deposition rate of PRR50504. The period (247 ka – 239 ka) with deposition rate of zero corresponds to the unconformity near the top of the sample. (F) Modeled meltwater production rates beneath Antarctica.

200

Though this subglacial precipitate records hydrologic and chemical conditions from a single location beneath EAIS, the sudden shift in precipitate textures across TIII (Fig. 1a) suggests that conditions in PRR50504 parent waters changed in response to a global climate event. Similar connections between the EAIS hydrologic system and Southern Hemisphere temperature change have been linked to catchment-scale basal meltwater flushing cycles driven by climate changes. (Piccione
205 et al., 2022). To investigate the hydrologic change in PRR50504, we first focus on the alternating, 200µm opal and calcite layers in the bottom section of the sample, which represent episodic shifts in precipitate parent water chemistry and/or physical

conditions in the subglacial aqueous environment. Previous investigations of Antarctic subglacial precipitates with interspersed opal and calcite layers presented evidence showing that their formation is tied to cycles of freezing and flushing of basal water (Piccione et al., 2022). Opal deposition requires high concentrations of Si in solution, interpreted to be occurring through

210   cryoconcentration of a fluid that is undersaturated with respect to calcite. Opal precipitation in the subglacial environment is slow, as it requires precipitation and settling of colloidal silica out of the water column. Subsequent flushing of CO_2-rich waters into the system switches precipitation to calcite until the solution is once again below the calcite saturation point (Piccione et al., 2022). Therefore, calcite accumulation is i) minimal during times when subglacial flushing rates are slow because CO_2 delivery is low, ii) highest when subglacial flushing increases, but iii) can become dampened if subglacial flushing rates

215   become so high that previously solute-rich, Ca-rich, subglacial waters are diluted with fresh glacial meltwater. Frequency analysis of the timeseries describing pre-TIII opal-calcite deposition show that these mineralogic transitions occur on a 150-650 yr frequency (Fig. 2d). There are no other glaciological (i.e. basal freezing/melting) or chemical (i.e. chemical weathering) processes that are both cyclic and can affect the basal hydrologic environment on a century-scale. Therefore, century-scale pacing of opal-calcite layer formation are interpreted here to indicate that these layers resulted from subglacial meltwater

220   flushing events in an active hydrologic system. That is, in the 15 kyr prior to TIII, ambient conditions in the subglacial environment where PRR50504 formed supported freezing of parent waters and opal precipitation, which was interrupted by centennially paced flooding of upstream waters that drove calcite precipitation. Basal meltwater flushing cycles of similar frequency are recorded in other calcite precipitates collected near Elephant Moraine, and are attributed to sequences of gradual filling and abrupt discharge from upstream subglacial lakes (Piccione et al., n.d.). Following TIII, opal layers in PRR50504

225   become less frequent –with only two thin 50-200 μm black-colored opal layers deposited in the upper section of the sample–
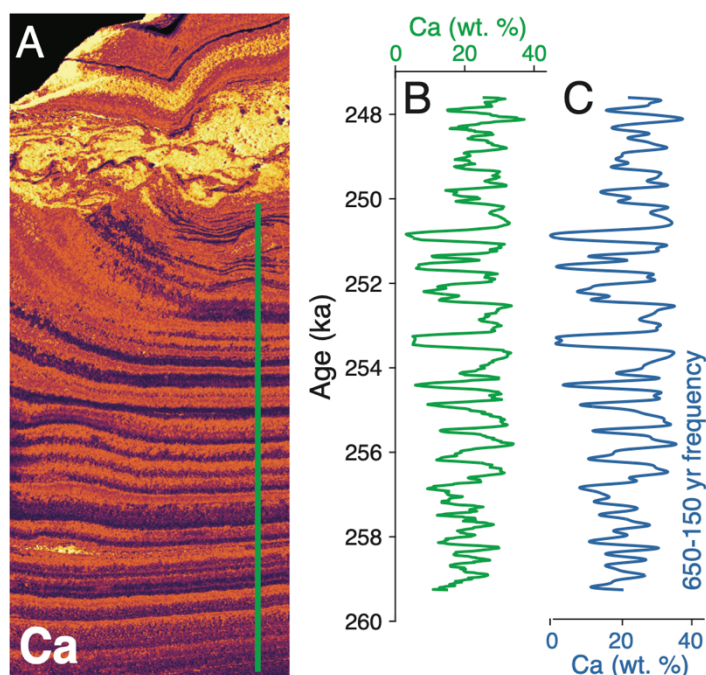
and the sample is made predominantly of red-brown calcite. Compared to the fine opal-calcite layering prior to the termination, the deposition rate of this post-TIII calcite is significantly slower (Fig. 1e), indicating that meltwater flushing to the sample formation area slowed as the climate cooled following TIII.

Figure 2: Pre-Termination III centennial-scale opal-calcite deposition. (**A**) Map of Ca measured with micro-XRF (μ-XRF). Green line represent area where line scan was measured in B. (**B**) Time series data of calcium concentration (wt%) in bottom segment of PRR50504. High Ca values represent carbonate layers; low Ca values represent opal layers. (**C**) Signal multiresolution analysis of spectra in B, including only frequencies between 650 and 150 yr. The close match between this spectrum and the one in B, suggests that the dominant depositional period of opal-calcite cycles is between 650 and 150 yr periods.

245

The isotopic compositions of both pre- and post-termination calcite layers fall in two distinct locations along a two-component mixing line in $\delta^{13}C$-$\delta^{18}O$, $\delta^{18}O$-$^{87}Sr/^{86}Sr$, and $[^{234}U/^{238}U]$-$^{87}Sr/^{86}Sr$ space, suggesting that they formed from a mixture of the same two parent waters (Fig. 3). Endmember isotopic compositions of these mixing models record information about the chemistry and provenance of the two waters. For example, since the $\delta^{18}O$ values of ice vary between the ice sheet

250   interior and margins (Werner et al., 2018), the oxygen isotope composition of precipitate parent waters can record the provenance of their meltwater source (Piccione et al., 2022). In PRR50504, the two endmember $\delta^{18}O$ values vary by ~11‰, between -46‰ and -57.5‰ (Fig. 3a). The lower endmember $\delta^{18}O$ value (-57.5‰) is similar in composition to snow at the EAIS domes, while the higher endmember $\delta^{18}O$ value (-46‰) is consistent with snow that originated in the EAIS peripheral region close to the sample collection location (Werner et al., 2018). Two component parent water mixtures with similar $\delta^{18}O$

255   values have been reported from other precipitates both at Elephant moraine and Mount Achernar (Piccione et al., 2022), and are interpreted as mixing of interior meltwaters with those along the ice sheet periphery. Based on this interpretation, hereafter we refer to the two endmembers as interior versus peripheral. The interior versus peripheral meltwaters also have distinct C, Sr, and U isotope compositions. Endmember $\delta^{13}C$ values (-23‰ in the interior, versus ~0‰ in the periphery) vary widely, and likely stem from different carbon source materials in the two areas of the ice sheet (Piccione et al., 2022). Similarly, $^{87}Sr/^{86}Sr$

260   values vary between 0.7125 and 0.7155 between the interior and peripheral endmembers respectively, suggesting that these two water sources have different bedrock types. Beyond the distinct endmember compositions, the shape of isotope mixing models is set by the elemental ratio between the two endmember waters, and thus bears on the relative abundance of O, C, U, and Sr in the two waters. The endmember water from the ice sheet periphery has higher $[^{234}U/^{238}U]$ values (2.65 versus 2.45 in the interior endmember) (Fig. 3b), and 100-fold higher Sr concentration than the interior endmember (Fig. 3b,c), indicative

265   of longer periods of water-rock interaction along the ice sheet margins (Blackburn et al., 2020). Carbonates deposited before TIII fall closer to the interior endmember, showing that the system was dominated by subglacial meltwater that flowed from the ice sheet interior prior to TIII. After TIII, PRR50504 carbonate isotopic compositions systematically shift towards the peripheral endmember, which indicates that the hydrologic connectivity between ice sheet periphery and its interior waned during post-termination cooling causing hydrologic isolation of precipitate parent waters. This type of subglacial hydrologic

270   development is expected when increasingly larger parts of the ice sheet bed are experiencing basal freezing, which may restrict or eliminate long-distance drainage pathways at the ice sheet bed. Onset of gradual cooling after a termination and an interglacial during which the ice sheet has thinned causes thermodynamic conditions that favor shifting of basal thermal regiment from melting to freezing.
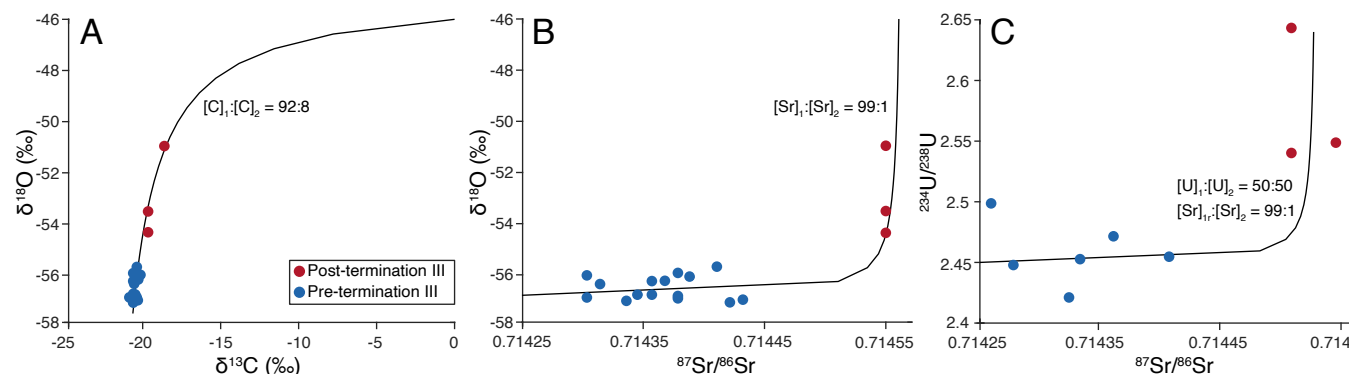
Figure 3. Two-component oxygen, carbon, strontium, and uranium isotope mixing models for PRR50504 carbonate layers. (A) PRR50504 carbonate data in $\delta^{18}O$ versus $\delta^{13}C$ space. (B) As in A, but in $\delta^{18}O$ versus $^{87}Sr/^{86}Sr$ space. (C) As in A and B, but in $[^{234}U/^{238}U]$ versus $^{87}Sr/^{86}Sr$ space. Markers represent individual carbonate measurements, with color representing their position in the sample, where blue markers represent carbonate deposited before TIII and red markers represent carbonate deposited after TIII. Black lines represent two-component mixing models that fit calcite data. Element concentration ratios between the two endmember waters from these mixing models are labelled. Endmember 1 is in the third quadrant each graph and endmember 2 is in the first quadrant.

3.2 Manganous Brine Formation Tied to Ice Dynamic Processes

The diminished Antarctic subglacial hydrologic activity following TIII not only drove slower deposition rates in PRR50504, but also triggered a significant shift in parent water chemistry (Fig. 4). In the pre-TIII bottom section of the sample, opal and carbonate contain little to no trace metals, save for one prominent layer with high Fe concentrations (Fig. 4). Elemental maps collected using micro-X-Ray fluorescence (μ-XRF) imaging show that this pre-TIII iron is concentrated in a single particulate-rich layer (Fig. 4b). Measurements of X-Ray absorption near edge structure (μ-XANES) spectra on these particles indicate that they are Fe (III)-rich silicates, consistent with detrital sediments (Fig. 5b). In the portion of PRR50504 deposited after TIII, laser ablation multi-collector inductively coupled mass spectrometry (LA ICP-MS) and μ-XRF analyses demonstrate enriched concentrations of redox sensitive trace elements including Fe, Mn, Cu, S, and Mo (Fig. 4b,c). In this upper section of the sample, Fe, Mn, and Cu are abundant in particles directly above the unconformity, as well as in the two black opal layers (Fig. 4b). However, the strongest enrichments of all five elements are found in the carbonate layers (Fig. 4b). Negative correlations between trace element concentrations and Si (Fig. S2), and a lack of association with Al (Fig. S3), provide further evidence that Fe, Mn, Cu, S, and Mo are concentrated in the carbonate precipitate itself, rather than in detrital grains or clays. Incorporation of these redox sensitive elements in the carbonate and opal layers is strong indication that they were present in high concentrations in the precipitate parent water.

Figure 4 (below). Elemental composition of sample PRR50504 measured with XRF and LA ICP-MS. (A) Plain light image of PRR50504. The green box delineates the location of Ca, Fe, Mn, and Cu μ-XRF maps in B; the blue box delineates the location of the Si and S μ-XRF maps in B; and the black box delineates the location of the LA ICP-MS analyses in C. **(B)** μ-XRF maps of Ca, Fe, Mn, Cu, Si, and S. **(C)** LA ICP-MS Ca, Fe, Mn, Cu, and Mo concentration analyses of calcite layers in PRR50504.
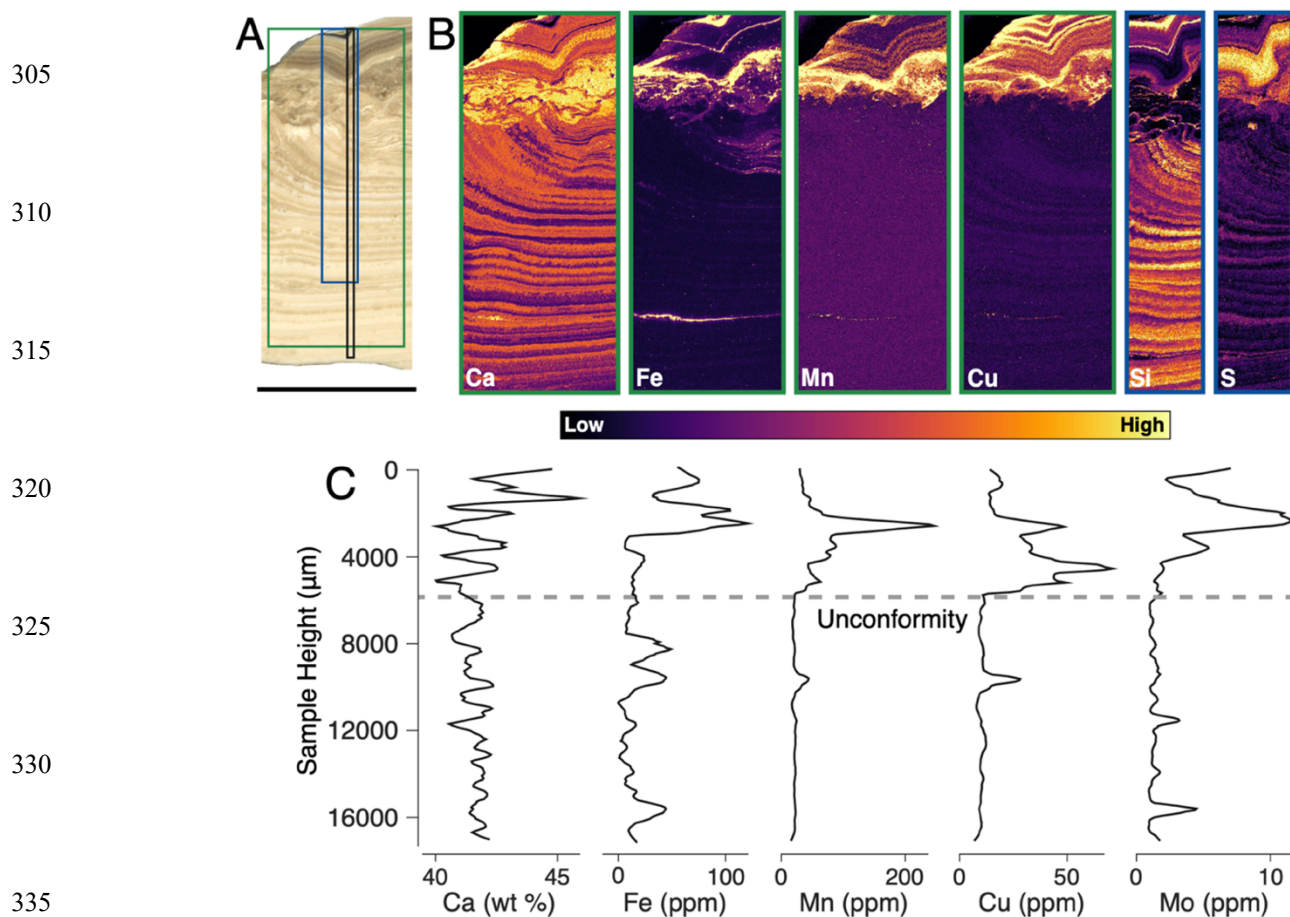
Mobilization of redox sensitive elements beneath ice sheets has been attributed to suboxic or anoxic fluids where chemolithotrophic organisms drive chemical weathering of trace-metal bearing phases (e.g. sulfides, Fe or Mn-oxides) (Wadham et al., 2010). In PRR50504, we measure the elemental concentrations of Fe, Mn, Cu, and Mo, paired with Fe, Mn, and S K-edge μ-XANES to explore the redox conditions in parent waters that led to the apparent trace metal cycling following TIII. First, Mn K-edge μ-XANES show that Mn-rich areas at the top of the sample are a Mn^{2+}-carbonate (Fig. 5c), formation of which requires reducing conditions where dissolution of Mn-oxides from the bedrock substrate drive high concentrations of Mn^{2+} in solution (Calvert and Pedersen, 1993). Second, Fe and Mn concentrations are of similar magnitude (Fig. 4c), indicating that both Fe and Mn were highly concentrated in the parent waters. Based on Fe K-edge μ-XANES, the detritus directly above the unconformity is mixed Fe^{2+} and Fe^{3+} silicates (Fig. 5b), consistent with glaciogenic sediments weathered in anoxic environments (Hawkings et al., 2018). Third, S K-edge μ-XANES show that high concentrations of sulfur (Fig. 4b) are present as sulfate (Fig. 5a), with no evidence for precipitated sulfides, meaning that parent waters did not become sufficiently anoxic to drive sulfate reduction (i.e. sulfidic or euxinic conditions). Finally, elevated Mo and Cu concentrations in the top of the sample coincide with high Mn and Fe concentrations (Fig. 4b,c; Fig. S6), consistent with Fe-Mn-oxide dissolution in a

350   manganous or ferruginous environment (Scott and Lyons, 2012; Tribovillard et al., 2006). Collectively, these experiments show that the subglacial waters were near the redox boundary between manganous and ferruginous conditions during the deposition of the top section of the sample. The manganous/ferruginous, sulfate-rich conditions that developed in PRR50504 parent waters following TIII match those in the groundwater brine beneath Taylor Glacier that is discharged from Blood Falls (Mikucki et al., 2015, 2009). The evidence presented here for high trace metal concentrations in subglacial waters beneath the

355   EAIS suggests that Blood-Falls-like fluids existed also in the subglacial aqueous system in which PRR50504 precipitated. Given the numerous instances and geographic distribution of metal-rich subglacial waters emanating from beneath ice in Antarctica (Annett et al., 2015b; Monien et al., 2017; Forsch et al., 2021), the hydrologically isolated, suboxic environments that produce these brines are likely ubiquitous beneath the ice sheet, particularly in its peripheral regions where lower ice thicknesses favor basal freezing (e.g., Pattyn, 2010). The transition in PRR50504 from redox element-poor meltwater prior to

360   TIII, to metal-rich parent waters after TIII indicates that these metal-rich brines can naturally form in subglacial environments in response to changing hydrological connectivity or isolation, which control the availability of oxygen in subglacial waters.
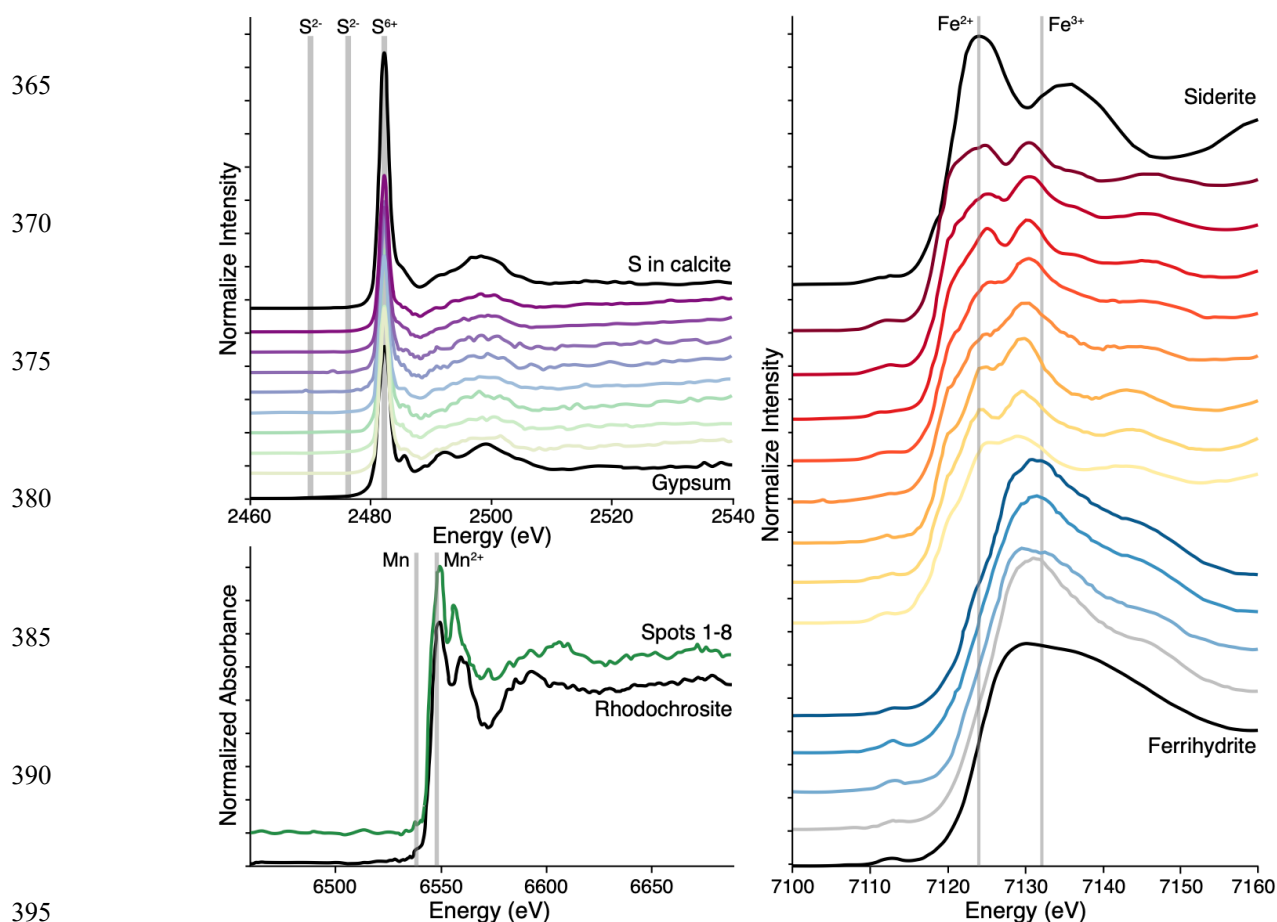
Figure 5 (above). S, Fe, and Mn K-edge Micro X-Ray Absorption Near Edge Structure (µ-XANES) spectra from PRR50504. (A) Sulfur K-edge µ-XANES from eight spots in the upper section of PRR50504. All areas measured have a peak energy position that matches sulfate (S^{2+}). Black spectra are sulfate-rich carbonate (top) and gypsum (bottom) sulfate reference standards. **(B)** Iron K-edge µ-XANES

400 from eleven spots in the upper section of PRR50504 (colored red to blue) and a spectrum from three spots from the lower section of PRR50504 (combined into the single grey spectrum). Black spectra are from an Fe^{2+} reference standard (siderite, top) and an Fe^{3+} standard (ferrihydrite, bottom). Red spectra from the upper portion of the sample have peaks at 7124 and 7132 eV that indicate mixed Fe^{2+} and Fe^{3+}. Blue and grey only have peaks at 7132eV indicating that they consist of just Fe^{3+}. **(C)** Mn K-edge µ-XANES from eight Mn-rich spots in the upper section of PRR50504 (combined in the green spectrum) and a Mn-carbonate standard (rhodochrosite, black spectrum). Both spectra

405 have weak pre-edge peak at 6539eV, and an edge position at 6549eV indicative of Mn^{2+} species(Schaub et al., 2023); the double peak structure is characteristic of rhombohedral carbonate (Lee et al., 2002).

3.3 Subglacial Trace Metal Mobilization Linked to Climate Through Basal Flushing Rates

To interpret the apparent link between the changes in Antarctic subglacial flushing rates recorded in PRR50504 and the broader Southern Hemisphere climate, we model the evolution of basal meltwater production across the period of time covered

410 by our sample. This model estimates how shear heating and conductive heat loss evolve during climate fluctuations and drive the heat budget of the ice-bed interface (Fig. 1e) (see Supplemental Materials section 1). Across the period of PRR50504 formation, the deposition rate (Fig. 1d) and depositional frequency of opal-carbonate layers (Fig. 2) respond to trends in basal meltwater production. From 258ka to 251ka, increased meltwater availability leading up to TIII (Fig. 1e) drove the frequent centennial-scale opal-calcite transitions (Fig. 2) and higher deposition rates (Fig. 1e). At 251ka the subglacial meltwater

415 production reached a threshold value that was large enough to dilute the precipitate parent water to the point where it was no longer saturated with respect to opal and carbonate, causing precipitate-formation to cease (Fig. 1e). Following the TIII, meltwater production beneath the thinned ice sheet experiencing renewed surface cooling decreased rapidly, isolating PRR50504 parent waters along the periphery of the ice sheet from upstream basal meltwater. Eventually, this isolation allowed the parent water to again become saturated with respect to carbonate and precipitate formation to restart, but the change in

420 meltwater delivery rate resulted in reducing conditions and distinct parent water chemistries.

The trends in subglacial flushing rates across TIII evident in PRR50504 (Fig. 1; Fig. 2) are interpreted here as resulting from climate-driven changes in the ice sheet thickness and dynamics that modulate subglacial meltwater and oxygen supply through their impact on conductive heat loss and basal shear heating (Fig. 1e) (see Supplemental Materials section 1). Similar climate-forced fluctuations in Antarctic subglacial hydrologic activity has been reported from precipitate samples covering a

425 range of Late Pleistocene climatic conditions outside of terminations (Piccione et al., 2022, n.d.). Pleistocene glacial terminations trigger rapid ice motion and thinning along the EAIS periphery (Wilson et al., 2018). Consequent subglacial shear heating and steepening of the ice surface gradient may have caused the highest influx of far-travelled meltwater to PRR50504 parent waters during TIII (Fig. 1e). Immediately following terminations ice motion slowed, but slow ice surface accumulation rates behind the Transantarctic Mountains imply that it takes many millennia to re-establish peak glacial ice thickness and

430 extent. This post-termination period of slow ice motion, thin ice, and low ice surface slopes along the Antarctic margins produced the lowest rates of subglacial meltwater production (Fig. 1e), and we interpret it as the cause of subglacial freezing and diminished meltwater flushing intensities recorded in our sample. The dataset presented here establishes this connection

between climate cycles and subglacial hydrology, where the weakened subglacial hydrologic activity following TIII facilitates the isolation of precipitate parent waters from upstream meltwaters.

435   3.4 Climate-Driven Trends in Antarctic Trace Metal Discharge to the Southern Ocean

Modern Antarctic basal waters have a range of Fe concentrations, ranging from Fe-poor, oxygenated waters (Vick-Majors et al., 2020) to suboxic, Fe-rich brines (Lyons et al., 2019). Modeling studies estimate modern Fe discharge rates of up to 1.4 Gmol yr^{-1} by extrapolating these observed water compositions to the ice sheet-scale (Hawkings et al., 2020), suggesting that basal meltwater may play an important role in fertilizing Southern Ocean ecosystems. The precipitate record presented here
440   offers the first well-dated geologic record illustrating how subglacial trace metal cycling may vary in response to orbital-scale climate fluctuations, permitting similar estimates of Antarctic Fe discharge to the Southern Ocean on orbital timescales.

We evaluate Antarctic Fe discharge rate across TIII by integrating results from our simplified model of meltwater discharge rate (Fig. 1e) with estimates of Fe concentration of subglacial waters, informed by the fluctuations in trace metal mobility observed our subglacial precipitate record (Fig. 6c). Similar to previous models of Antarctic Fe discharge flux
445   (Hawkings et al., 2020), this calculation is limited by the necessity to extrapolate observed water compositions to the continent-wide basal hydrologic system. Hence, we investigate the sensitivity of Antarctic Fe flux to a range of meltwater Fe concentrations, representing the possible influence of climate-driven changes in subglacial trace metal mobility on Antarctic Fe discharge to the Southern Ocean.

Prior to TIII, PRR50504 parent waters had low trace metal concentrations, indicative of oxidized aqueous conditions. To
450   simulate discharge of this Fe-poor waters, we set basal meltwater Fe concentration to those in modern Subglacial Lake Whillans (2504nM Fe) (Vick-Majors et al., 2020) for the 15 kyr prior to TIII. Calculated Fe flux aligns with meltwater discharge rates in this pre-TIII period, increasing from 0.15 Gmol yr^{-1} before the termination up to 0.33 Gmol yr^{-1} during the termination (Fig. 6c). These values are consistent with previous estimates of Fe discharge that assume lower Fe concentrations in subglacial waters (Hawkings et al., 2014; Hodson et al., 2017), but are below an estimate of 1.4 Gmol yr^{-1} made using Fe
455   concentrations of Subglacial Lake Mercer (Hawkings et al., 2020). As the climate cooled following TIII, PRR50504 parent waters become manganous/ferruginous, exhibiting a trace metal composition akin to that of modern Blood Falls brines (Lyons et al., 2019). To represent the subglacial formation of Fe-rich waters in the 10 kyr after TIII, we set subglacial meltwater Fe concentrations for this period equal to a mixture of Subglacial Lake Whillans compositions plus a varying portion (ranging between plausible but arbitrarily selected range of values between 0.001 and 0.005%) of Blood Falls brines. The magnitude of
460   Fe discharged from beneath the Antarctic Ice Sheet is highly sensitive to this increase in meltwater Fe concentration, with average Fe flux maintaining peak termination values of approximately 0.3 Gmol yr^{-1} when just 0.001% of subglacial waters contain Fe concentrations equal to Blood Falls values. Total Fe flux increases by about 0.2 Gmol yr^{-1} for every 0.001% increase in the fraction of basal water made up of Fe-rich brine, and increasing by an order of magnitude when subglacial waters contain 0.005% brine (Fig. 6c). These Fe flux estimates demonstrate that the increase in subglacial trace metal mobility beneath the

465   Antarctic ice sheet following glacial terminations can significantly increase the subglacial meltwater Fe flux to the Southern Ocean.

     Parent water compositions from PRR50504 represent conditions in just one area of the subglacial environment. Therefore, Fe flux estimates are intended only to schematically illustrate the relative change in Fe discharge that may occur due to the emergence of widespread suboxic basal conditions following glacial terminations. However, the transition from centennial-

470   scale subglacial flushing in PRR50504 parent waters before TIII, to hydrologically more isolated conditions post-termination stems from a shift in the Antarctic basal hydrologic system in response to ice dynamic changes following the TIII. Previous studies have noted a comparable response of subglacial waters to Southern Hemisphere climate events, evident in various locations across the EAIS, indicating a catchment-wide phenomenon (Piccione et al., 2022). Therefore, the hydrologic shift that drove increased trace metal mobility following TIII may have can occur throughout the Antarctic periphery, and thus may

475   significantly increase Fe flux to the Southern Ocean during this period.
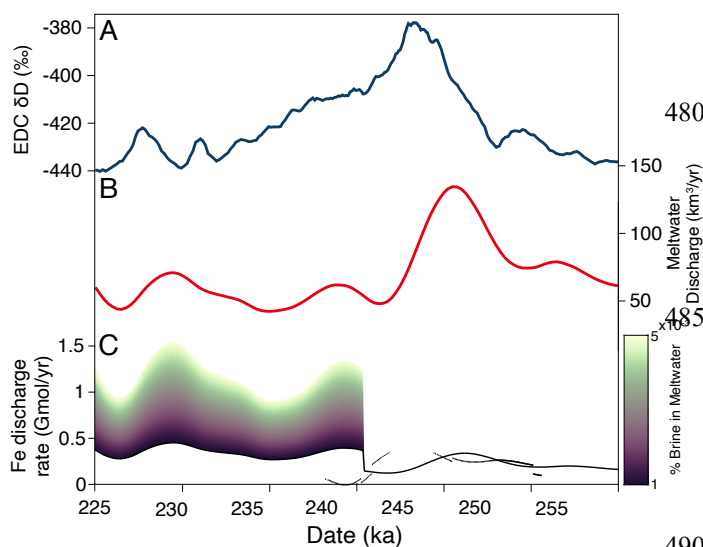

Figure 6. Simplified model of Antarctic subglacial Fe flux across TIII. **(A)** δD measured in the EPICA Dome C Ice Core **(Jouzel et al., 2007; Veres et al., 2013)**. **(B)** Modeled meltwater production rates beneath Antarctica. **(C)** Modeled Antarctic subglacial Fe flux. Color scale represents the fraction of subglacial meltwater made up of brine compositions.

     The precipitate record presented here demonstrates increased subglacial trace metal mobility arising along the Antarctic periphery following glacial terminations, which can lead to enhanced Fe flux to the Southern Ocean during a transition from interglacial to glacial conditions. Nutrients sourced from the Antarctic basal environment have been shown to be highly bioavailable, meaning that this meltwater flux can

490 enhance marine productivity in regions where it is discharged (Hawkings et al., 2018, 2014). In the Antarctic zone of the Southern Ocean, nutrient supply is influenced from above (i.e. dust, iceberg rafted detritus, and Antarctic meltwater) and below (i.e. upwelling of nutrient-dense bottom waters). Elemental and isotope analyses of marine sediment records from the Antarctic zone reveal that a shift from high upwellings during the warmest climate periods to stratification during glacial periods is the

495 main driver of changes in primary productivity on orbital timescales (Studer et al., 2015; Sigman et al., 2021). As stratification increases in the Antarctic zone nitrate consumption in the surface ocean becomes more complete, suggesting the need for additional iron sources beyond deep marine Fe (Studer et al., 2015). While current data do not allow for an unequivocal identification of these Fe sources, increased Fe flux from Antarctic meltwater during climate cooling represents a potential origin for these nutrients.

4 Conclusions

Our record of Antarctic subglacial hydrochemistry across TIII suggests that ice dynamic response to rapid warming during the termination increased the delivery of fresh meltwater flushing to the ice sheet margins. As climate cooled from peak termination temperatures, reduced ice motion, shallow ice sheet surface slope, and thinner ice reduced subglacial meltwater production and flushing, leading to increased hydrologic isolation of subglacial waters on the ice sheet periphery from the broader hydrologic system in the ice sheet interior. The consequent reduction in oxygen supply to peripheral subglacial waters favored manganous/ferruginous conditions and high concentrations of trace metals in the precipitate parent water. These post-TIII conditions in PRR50504 are geochemically akin to those in the modern Blood Falls brine, suggesting that such suboxic fluids with high concentrations of Fe and other transition metals can be common in subglacial environments proximal to ice sheet margins.

Collectively, our data demonstrate that climate change, ice motion, and hydrologic flushing intensity play a role in regulating the mobility of trace metals beneath the Antarctic ice sheet. On this basis, trace metal flux in Antarctic subglacial meltwaters is likely highest as the climate cools over a thinned and slow-moving ice sheet during the transition from interglacial to glacial periods. Warm climate periods favor increased subglacial meltwater production and flushing with more oxygenated conditions and reduced mobility of redox sensitive elements in the subglacial waters. In particular, before and during terminations, subglacial water discharge may be much more voluminous than after terminations, but such discharge is also likely to contain relatively dilute concentrations of Fe and other transition metals. Given the speculation that Antarctic meltwater discharge can fertilize Southern Ocean ecosystems (Death et al., 2014), our dataset linking Antarctic subglacial trace metal flux with climate-related basal meltwater production may have significant implications for modelling the role that Antarctic micronutrients play in the carbon cycle on glacial-interglacial timescales as it suggests that trace metal output from the ice sheet can vary by orders of magnitude with climate conditions. Our current findings suggest that such output may be the highest during onset of post-interglacial cold conditions, which may help promote carbon burial in the Southern Ocean and potentially aid the lowering of the atmospheric carbon-dioxide concentration that pushes the climate system towards increasingly colder state.

16

References

Alderkamp, A. C., Mills, M. M., van Dijken, G. L., Laan, P., Thuróczy, C. E., Gerringa, L. J. A., de Baar, H. J. W., Payne, C. D., Visser, R. J. W., Buma, A. G. J., and Arrigo, K. R.: Iron from melting glaciers fuels phytoplankton blooms in the Amundsen Sea (Southern Ocean): Phytoplankton characteristics and productivity, Deep-Sea Res. Part II Top. Stud. Oceanogr., 71–76, 32–48, https://doi.org/10.1016/j.dsr2.2012.03.005, 2012.

Annett, A. L., Skiba, M., Henley, S. F., Venables, H. J., Meredith, M. P., Statham, P. J., and Ganeshram, R. S.: Comparative roles of upwelling and glacial iron sources in Ryder Bay, coastal western Antarctic Peninsula, Mar. Chem., 176, 21–33, https://doi.org/10.1016/j.marchem.2015.06.017, 2015a.

Annett, A. L., Skiba, M., Henley, S. F., Venables, H. J., Meredith, M. P., Statham, P. J., and Ganeshram, R. S.: Comparative roles of upwelling and glacial iron sources in Ryder Bay, coastal western Antarctic Peninsula, Mar. Chem., 176, 21–33, https://doi.org/10.1016/j.marchem.2015.06.017, 2015b.

Balaguer, J., Koch, F., Hassler, C., and Trimborn, S.: Iron and manganese co-limit the growth of two phytoplankton groups dominant at two locations of the Drake Passage, Commun. Biol., 5, 1–12, https://doi.org/10.1038/s42003-022-03148-8, 2022.

Blackburn, T., Edwards, G. H., Tulaczyk, S., Scudder, M., Piccione, G., Hallet, B., McLean, N., Zachos, J. C., Cheney, B., and Babbe, J. T.: Ice retreat in Wilkes Basin of East Antarctica during a warm interglacial, Nature, 583, 554–559, https://doi.org/10.1038/s41586-020-2484-5, 2020.

Browning, T. J., Achterberg, E. P., Engel, A., and Mawji, E.: Manganese co-limitation of phytoplankton growth and major nutrient drawdown in the Southern Ocean, Nat. Commun., 12, 1–9, https://doi.org/10.1038/s41467-021-21122-6, 2021.

565 Calvert, S. E. and Pedersen, T. F.: Geochemistry of Recent oxic and anoxic marine sediments: Implications for the geological record, Mar. Geol., 113, 67–88, https://doi.org/10.1016/0025-3227(93)90150-T, 1993.

Cheng, H., Edwards, R. L., Hoff, J., Gallup, C. D., Richards, D. A., and Asmerom, Y.: The half-lives of uranium-234 and thorium-230, Chem. Geol., 169, 17–33, 2000.

Coplen, T. B., Brand, W. A., Gehre, M., Grhning, M., Meljer, L. H. A. J., Toman, B., and Verkouteren, R. M.: New Guidelines
570 for δ13C Measurements, Anal. Chem., 78, 2439–2441, 2006.

Death, R., Wadham, J. L., Monteiro, F., Le Brocq, A. M., Tranter, M., Ridgwell, A., Dutkiewicz, S., and Raiswell, R.: Antarctic ice sheet fertilises the Southern Ocean, Biogeosciences, 11, 2635–2643, https://doi.org/10.5194/bg-11-2635-2014, 2014.

Dold, B., Aguilera, a, Cisternas, M. E., Bucchi, F., and Amils, R.: Sources for Iron Cycling in the Southern Ocean, Environ. Sci. Technol., 47, 6129–6136, 2013.

575 Forsch, K. O., Hahn-Woernle, L., Sherrell, R. M., Roccanova, V. J., Bu, K., Burdige, D., Vernet, M., and Barbeau, K. A.: Seasonal dispersal of fjord meltwaters as an important source of iron and manganese to coastal Antarctic phytoplankton, Biogeosciences, 18, 6349–6375, https://doi.org/10.5194/bg-18-6349-2021, 2021.

Frisia, S., Weyrich, L. S., Hellstrom, J., Borsato, A., Golledge, N. R., Anesio, A. M., Bajo, P., Drysdale, R. N., Augustinus, P. C., Rivard, C., and Cooper, A.: The influence of Antarctic subglacial volcanism Maximum, Nat. Commun., 8, 1–9,
580 https://doi.org/10.1038/ncomms15425, 2017.

Gerringa, L. J. A., Alderkamp, A. C., Laan, P., Thuróczy, C. E., De Baar, H. J. W., Mills, M. M., van Dijken, G. L., Haren, H. van, and Arrigo, K. R.: Iron from melting glaciers fuels the phytoplankton blooms in Amundsen Sea (Southern Ocean): Iron biogeochemistry, Deep-Sea Res. Part II Top. Stud. Oceanogr., 71–76, 16–31, https://doi.org/10.1016/j.dsr2.2012.03.007, 2012.

Goodwin, I. D.: The nature and origin of a jokulhlaup near Casey Station, Antarctica, J. Glaciol., 34, 95–101,
585 https://doi.org/10.1017/S0022143000009114, 1988.

Hamelin, B., Bard, E., Zindler, A., and Fairbanks, R. G.: 234U238U mass spectrometry of corals: How accurate is the UTh age of the last interglacial period?, Earth Planet. Sci. Lett., 106, 169–180, https://doi.org/10.1016/0012-821X(91)90070-X, 1991.

Hawkings, J. R., Wadham, J. L., Tranter, M., Raiswell, R., Benning, L. G., Statham, P. J., Tedstone, A., Nienow, P., Lee, K.,
590 and Telling, J.: Ice sheets as a significant source of highly reactive nanoparticulate iron to the oceans, Nat. Commun., 5, 3929, https://doi.org/10.1038/ncomms4929, 2014.

Hawkings, J. R., Benning, L. G., Raiswell, R., Kaulich, B., Araki, T., Abyaneh, M., Stockdale, A., Koch-Müller, M., Wadham, J. L., and Tranter, M.: Biolabile ferrous iron bearing nanoparticles in glacial sediments, Earth Planet. Sci. Lett., 493, 92–101, https://doi.org/10.1016/j.epsl.2018.04.022, 2018.

595 Hawkings, J. R., Skidmore, M. L., Wadham, J. L., Priscu, J. C., Morton, P. L., and Hatton, J. E.: Enhanced trace element mobilization by Earth's ice sheets, Proc. Natl. Acad. Sci., 1–12, https://doi.org/10.1073/pnas.2014378117, 2020.

Herraiz-Borreguero, L., Lannuzel, D., van der Merwe, P., Treverrow, A., and Pedro, J. B.: Large flux of iron from the Amery Ice Shelf marine ice to Prydz Bay, East Antarctica, J. Geophys. Res. Oceans, 121, 6009–6020, https://doi.org/10.1002/2016JC011687, 2016.

600   Hodson, A., Nowak, A., Sabacka, M., Jungblut, A., Navarro, F., Pearce, D., Ávila-Jiménez, M. L., Convey, P., and Vieira, G.:
       Climatically sensitive transfer of iron to maritime Antarctic ecosystems by surface runoff, Nat. Commun., 8, 1–7,
       https://doi.org/10.1038/ncomms14499, 2017.

       Jaccard, S. L., Galbraith, E. D., Martínez-Garciá, A., and Anderson, R. F.: Covariation of deep Southern Ocean oxygenation
       and atmospheric CO2 through the last ice age, Nature, 530, 207–210, https://doi.org/10.1038/nature16514, 2016.

605   Jouzel, J., Masson-Delmotte, V., Cattani, O., Dreyfus, G., Falourd, S., Hoffmann, G., Minster, B., Nouet, J., Barnola, J. M.,
       Chappellaz, J., Fischer, H., Gallet, J. C., Johnsen, S., Leuenberger, M., Loulergue, L., Luethi, D., Oerter, H., Parrenin, F.,
       Raisbeck, G., Raynaud, D., Schilt, A., Schwander, J., Selmo, E., Souchez, R., Spahni, R., Stauffer, B., Steffensen, J. P., Stenni,
       B., Stocker, T. F., Tison, J. L., Werner, M., and Wolff, E. W.: Orbital and millennial antarctic climate variability over the past
       800,000 years, Science, 317, 793–796, https://doi.org/10.1126/science.1141038, 2007.

610   Kassab, C. M., Licht, K. J., Petersson, R., Lindbäck, K., Graly, J. A., and Kaplan, M. R.: Formation and evolution of an
       extensive blue ice moraine in central Transantarctic Mountains, Antarctica, J. Glaciol., 66, 49–60,
       https://doi.org/10.1017/jog.2019.83, 2019.

       Keller, B.: A Bayesian framework for integrated eruption age and age-depth modelling,
       https://doi.org/10.17605/OSF.IO/TQX3F, 2018.

615   Landschützer, P., Gruber, N., Haumann, F. A., Rödenbeck, C., Bakker, D. C. E., van Heuven, S., Hoppema, M., Metzl, N.,
       Sweeney, C., Takahashi, T., Tilbrook, B., and Wanninkhof, R.: The reinvigoration of the Southern Ocean carbon sink, Science,
       349, 1221–1224, https://doi.org/10.1126/science.aab2620, 2015.

       Lee, Y. J., Reeder, R. J., Wenskus, R. W., and Elzinga, E. J.: Structural relaxation in the MnCO3-CaCo3 solid solution: A Mn
       K-edge EXAFS study, Phys. Chem. Miner., 29, 585–594, https://doi.org/10.1007/s00269-002-0274-2, 2002.

620   Livingstone, S. J., Li, Y., Rutishauser, A., Sanderson, R. J., Winter, K., Mikucki, J. A., Björnsson, H., Bowling, J. S., Chu,
       W., Dow, C. F., Fricker, H. A., McMillan, M., Ng, F. S. L., Ross, N., Siegert, M. J., Siegfried, M., and Sole, A. J.: Subglacial
       lakes and their changing role in a warming climate, Nat. Rev. Earth Environ., 3, 106–124, https://doi.org/10.1038/s43017-021-
       00246-9, 2022.

       Llubes, M., Lanseau, C., and Rémy, F.: Relations between basal condition, subglacial hydrological networks and geothermal
625   flux in Antarctica, Earth Planet. Sci. Lett., 241, 655–662, https://doi.org/10.1016/j.epsl.2005.10.040, 2006.

       Lyons, W. B., Mikucki, J. A., German, L. A., Welch, K. A., Welch, S. A., Gardner, C. B., Tulaczyk, S. M., Pettit, E. C.,
       Kowalski, J., and Dachwald, B.: The Geochemistry of Englacial Brine From Taylor Glacier, Antarctica, J. Geophys. Res.
       Biogeosciences, 124, 633–648, https://doi.org/10.1029/2018JG004411, 2019.

       Martin, J. H.: Glacial-interglacial CO 2 change: The Iron Hypothesis, Paleoceanography, 5, 1–13,
630   https://doi.org/10.1029/PA005i001p00001, 1990.

       Martínez-Garcia, A., Rosell-Melé, A., Jaccard, S. L., Geibert, W., Sigman, D. M., and Haug, G. H.: Southern Ocean dust-
       climate coupling over the past four million years, Nature, 476, 312–315, https://doi.org/10.1038/nature10310, 2011.

       Martínez-García, A., Sigman, D. M., Ren, H., Anderson, R. F., Straub, M., Hodell, D. A., Jaccard, S. L., Eglinton, T. I., and
       Haug, G. H.: Iron fertilization of the subantarctic ocean during the last ice age, Science, 343, 1347–1350,
635   https://doi.org/10.1126/science.1246848, 2014.

Mikucki, J. A., Pearson, A., Johnston, D. T., Turchyn, A. V., Farquhar, J., Schrag, D. P., Anbar, A. D., Priscu, J. C., and Lee, P. A.: A Contemporary Microbially Maintained Subglacial Ferrous "Ocean," Science, 663, 397–401, 2009.

Mikucki, J. A., Auken, E., Tulaczyk, S., Virginia, R. A., Schamper, C., Sørensen, K. I., Doran, P. T., Dugan, H., and Foley, N.: Deep groundwater and potential subsurface habitats beneath an Antarctic dry valley, Nat. Commun., 6, https://doi.org/10.1038/ncomms7831, 2015.

Monien, D., Monien, P., Brünjes, R., Widmer, T., Kappenberg, A., Silva Busso, A. A., Schnetger, B., and Brumsack, H. J.: Meltwater as a source of potentially bioavailable iron to Antarctica waters, Antarct. Sci., 29, 277–291, https://doi.org/10.1017/S095410201600064X, 2017.

Northrup, P.: The TES beamline (8-BM) at NSLS-II : tender-energy spatially resolved X-ray absorption spectroscopy and X-ray fluorescence imaging, J. Synchrotron Radiat., 1–11, https://doi.org/10.1107/S1600577519012761, 2019.

Ostermann, D. R. and Curry, W. B.: Calibration of stable isotopic data: An enriched δ18O standard used for source gas mixing detection and correction, Paleoceanography, 15, 353–360, https://doi.org/10.1029/1999PA000411, 2000.

Paton, C., Hellstrom, J., Paul, B., Woodhead, J., and Hergtb, J.: Iolite : Freeware for the visualisation and processing of mass spectrometric data, J. Anal. At. Spectrom., 26, 2508–2518, https://doi.org/10.1039/c1ja10172b, 2011.

Pattyn, F.: Antarctic subglacial conditions inferred from a hybrid ice sheet / ice stream model, Earth Planet. Sci. Lett., 295, 451–461, https://doi.org/10.1016/j.epsl.2010.04.025, 2010.

Piccione, G., Blackburn, T., Tulaczyk, S., Rasbury, E. T., Hain, M. P., Ibarra, D. E., Methner, K., Tinglof, C., Cheney, B., Northrup, P., and Licht, K.: Subglacial precipitates record Antarctic ice sheet response to late Pleistocene millennial climate cycles, Nat. Commun., 13, 5428, https://doi.org/10.1038/s41467-022-33009-1, 2022.

Piccione, G., Pinter, S., Blackburn, T., Tulaczyk, S., and Rasbury, T.: Accelerated Antarctic ice loss through ocean forced changes in subglacial hydrology, Rev., n.d.

Priscu, J. C., Kalin, J., Winans, J., Campbell, T., Siegfried, M. R., Skidmore, M., Dore, J. E., Leventer, A., Harwood, D. M., Duling, D., Zook, R., Burnett, J., Gibson, D., Krula, E., Mironov, A., McManis, J., Roberts, G., Rosenheim, B. E., Christner, B. C., Kasic, K., Fricker, H. A., Lyons, W. B., Barker, J., Bowling, M., Collins, B., Davis, C., Gagnon, A., Gardner, C., Gustafson, C., Kim, O. S., Li, W., Michaud, A., Patterson, M. O., Tranter, M., Venturelli, R., Vick-Majors, T., and Elsworth, C.: Scientific access into Mercer Subglacial Lake: Scientific objectives, drilling operations and initial observations, Ann. Glaciol., https://doi.org/10.1017/aog.2021.10, 2021.

Raiswell, R., Benning, L. G., Tranter, M., and Tulaczyk, S.: Bioavailable iron in the Southern Ocean: The significance of the iceberg conveyor belt, Geochem. Trans., 9, 1–9, https://doi.org/10.1186/1467-4866-9-7, 2008.

Raiswell, R., Hawkings, J. R., Benning, L. G., Baker, A. R., Death, R., Albani, S., Mahowald, N., Krom, M. D., Poulton, S. W., Wadham, J., and Tranter, M.: Potentially bioavailable iron delivery by iceberg-hosted sediments and atmospheric dust to the polar oceans, Biogeosciences, 13, 3887–3900, https://doi.org/10.5194/bg-13-3887-2016, 2016.

Ravel, B. and Newville, M.: ATHENA , ARTEMIS , HEPHAESTUS : data analysis for X-ray absorption spectroscopy using IFEFFIT, J. Synchrotron Radiat., 12, 537–541, https://doi.org/10.1107/S0909049505012719, 2005.

Sabine, C. L., Feely, R. A., Gruber, N., Key, R. M., Lee, K., Bullister, J. L., Wanninkhof, R., Wong, C. S., Wallace, D. W. R., Tilbrook, B., Millero, F. J., Peng, T.-H., Kozyr, A., Ono, T., and Rios, A. F.: The Oceanic Sink for Anthropogenic CO 2, Science, 305, 367–371, https://doi.org/10.1126/science.1097403, 2004.

Schaub, D. R., Northrup, P., Nekvasil, H., Catalano, T., and Tappero, R.: Gas-mediated trace element incorporation into rhyolite-hosted topaz: A synchrotron microbeam XAS study, Am. Mineral., 108, 2153–2163, https://doi.org/10.2138/am-675   2022-8417, 2023.

Scott, C. and Lyons, T. W.: Contrasting molybdenum cycling and isotopic properties in euxinic versus non-euxinic sediments and sedimentary rocks: Refining the paleoproxies, Chem. Geol., 324–325, 19–27, https://doi.org/10.1016/j.chemgeo.2012.05.012, 2012.

Shoenfelt, E. M., Winckler, G., Lamy, F., Anderson, R. F., and Bostick, B. C.: Highly bioavailable dust-borne iron delivered 680   to the Southern Ocean during glacial periods, Proc. Natl. Acad. Sci., 115, 11180–11185, https://doi.org/10.1073/pnas.1809755115, 2018.

Sigman, D. M., Hain, M. P., and Haug, G. H.: The polar ocean and glacial cycles in atmospheric CO2 concentration, Nature, 466, 47–55, https://doi.org/10.1038/nature09149, 2010.

Sigman, D. M., Fripiat, F., Studer, A. S., Kemeny, P. C., Martínez-García, A., Hain, M. P., Ai, X., Wang, X., Ren, H., and 685   Haug, G. H.: The Southern Ocean during the ice ages: A review of the Antarctic surface isolation hypothesis, with comparison to the North Pacific, Quat. Sci. Rev., 254, 106732, https://doi.org/10.1016/j.quascirev.2020.106732, 2021.

Skidmore, M., Tranter, M., Tulaczyk, S., and Lanoil, B.: Hydrochemistry of ice steams beds- evaporitic or microbial effects?, Hydrol. Process., 24, 517–523, https://doi.org/10.1002/hyp, 2010.

Studer, A. S., Sigman, D. M., Martínez-García, A., Benz, V., Winckler, G., Kuhn, G., Esper, O., Lamy, F., Jaccard, S. L., 690   Wacker, L., Oleynik, S., Gersonde, R., and Haug, G. H.: Antarctic Zone nutrient conditions during the last two glacial cycles, Paleoceanography, 30, 845–862, https://doi.org/10.1002/2014PA002745, 2015.

Tribovillard, N., Algeo, T. J., Lyons, T., and Riboulleau, A.: Trace metals as paleoredox and paleoproductivity proxies: An update, Chem. Geol., 232, 12–32, https://doi.org/10.1016/j.chemgeo.2006.02.012, 2006.

Tulaczyk, S., Mikucki, J. A., Siegfried, M. R., Priscu, J. C., Barcheck, C. G., Beem, L. H., Behar, A., Burnett, J., Christner, B. 695   C., Fisher, A. T., Fricker, H. A., Mankoff, K. D., Powell, R. D., Rack, F., Sampson, D., Scherer, R. P., and Schwartz, S. Y.: WISSARD at Subglacial Lake Whillans, West Antarctica: Scientific operations and initial observations, Ann. Glaciol., 55, 51–58, https://doi.org/10.3189/2014AoG65A009, 2014.

Veres, D., Bazin, L., Landais, A., Toyé Mahamadou Kele, H., Lemieux-Dudon, B., Parrenin, F., Martinerie, P., Blayo, E., Blunier, T., Capron, E., Chappellaz, J., Rasmussen, S. O., Severi, M., Svensson, A., Vinther, B., and Wolff, E. W.: The 700   Antarctic ice core chronology (AICC2012): An optimized multi-parameter and multi-site dating approach for the last 120 thousand years, Clim. Past, 9, 1733–1748, https://doi.org/10.5194/cp-9-1733-2013, 2013.

Vick-Majors, T. J., Mitchell, A. C., Achberger, A. M., Christner, B. C., Dore, J. E., Michaud, A. B., Mikucki, J. A., Purcell, A. M., Skidmore, M. L., Priscu, J. C., Adkins, W. P., Anandakrishnan, S., Barbante, C., Barcheck, G., Beem, L., Behar, A., Beitch, M., Bolsey, R., Branecky, C., Edwards, R., Fisher, A., Fricker, H. A., Foley, N., Guthrie, B., Hodson, T., Horgan, H., 705   Jacobel, R., Kelley, S., Mankoff, K. D., McBryan, E., Powell, R., Sampson, D., Scherer, R., Siegfried, M., and Tulaczyk, S.: Physiological ecology of microorganisms in subglacial lake whillans, Front. Microbiol., 7, 1–16, https://doi.org/10.3389/fmicb.2016.01705, 2016.

Vick-Majors, T. J., Michaud, A. B., Skidmore, M. L., Turetta, C., Barbante, C., Christner, B. C., Dore, J. E., Christianson, K., Mitchell, A. C., Achberger, A. M., Mikucki, J. A., and Priscu, J. C.: Biogeochemical Connectivity Between Freshwater 710   Ecosystems beneath the West Antarctic Ice Sheet and the Sub-Ice Marine Environment, Glob. Biogeochem. Cycles, 34, https://doi.org/10.1029/2019GB006446, 2020.

Wadham, J. L., Tranter, M., Skidmore, M., Hodson, A. J., Priscu, J., Lyons, W. B., Sharp, M., Wynn, P., and Jackson, M.: Biogeochemical weathering under ice: Size matters, Glob. Biogeochem. Cycles, 24, https://doi.org/10.1029/2009GB003688, 2010.

715 Wadham, J. L., Hawkings, J. R., Tarasov, L., Gregoire, L. J., Spencer, R. G. M., Gutjahr, M., Ridgwell, A., and Kohfeld, K. E.: Ice sheets matter for the global carbon cycle, Nat. Commun., 10, https://doi.org/10.1038/s41467-019-11394-4, 2019.

Webster, J. G.: Trace-metal behaviour in oxic and anoxic CaCl brines of the Wright Valley drainage, Antarctica, Chem. Geol., 112, 255–274, https://doi.org/10.1016/0009-2541(94)90028-0, 1994.

Werner, M., Jouzel, J., Masson-Delmotte, V., and Lohmann, G.: Reconciling glacial Antarctic water stable isotopes with ice 720 sheet topography and the isotopic paleothermometer, Nat. Commun., 9, 1–10, https://doi.org/10.1038/s41467-018-05430-y, 2018.

Wilson, D. J., Bertram, R. A., Needham, E. F., van de Flierdt, T., Welsh, K. J., McKay, R. M., Mazumder, A., Riesselman, C. R., Jimenez-Espejo, F. J., and Escutia, C.: Ice loss from the East Antarctic Ice Sheet during late Pleistocene interglacials, Nature, 561, 383–386, https://doi.org/10.1038/s41586-018-0501-8, 2018.

725 Wróblewski, W., Gradziński, M., Motyka, J., and Stankovič, J.: Recently growing subaqueous flowstones: Occurrence, petrography, and growth conditions, Quat. Int., 437, 84–97, https://doi.org/10.1016/j.quaint.2016.10.006, 2017.